Anisotropic quantum six-vertex model on the square lattice

Márk Kondákor
BSc Physics Student
Budapest University of Technology and Economics

Supervisor: Karlo Penc
Institute of Solid State Physics and Optics
Wigner Research Centre for Physics

October 28, 2021
Corrected version: November 27, 2021

This work was submitted to the Students' Scientific Conference of
Faculty of Natural Sciences of Budapest University of Technology and Economics.

Abstract

Spin ice materials are rare-earth compounds where the Ising-like magnetic moments form a lattice of corner-shared tetrahedra (pyrochlore lattice), and the spin configurations at low temperatures follow the 2-in/2-out ice rule. The degeneracy of the ground-state ice manifold increases algebraically with the number of spins, providing a finite residual entropy, just like in the water ice. The ice manifold supports magnetic monopole-like excitations. The spin ice physics also arises in artificial spin ices, where single-domain nanomagnets are arranged in specific structures and coupled by their dipolar magnetic fields. Recently, a lattice of coupled superconducting flux qubits [1] realized a new type of artificial systems, where quantum effects are also present.

Inspired by this quantum artificial spin ice system, I study the phase diagram of the "anisotropic" quantum six-vertex model on the square lattice. The six vertices represent the 2-in/2-out configurations in the spin ice. In the model, the two types of vertices have a different energy, quantum fluctuations are taken into account by off-diagonal terms flipping the arrows along the sides of a square plaquette, and a corresponding diagonal part extends the Hamiltonian to a Rokhsar-Kivelson-like model. In the absence of the quantum flipping term, the classical phase diagram consists of three phases – a 2-fold degenerate totally flippable phase, a 4-fold degenerate phase optimizing for the energy of the vertices, and a manifold with non-flippable states. The introduction of the flipping terms leads to a plaquette phase of arrows resonating on alternating squares [2]. I determined phase boundaries for the quantum model analytically using variational and perturbational techniques and numerically by exact diagonalization of clusters having up to 72 spins.

Contents

1 Introduction

1.1 The water and spin ice

In the water ice crystal, the O^{2-} ions form a lattice of coordination four, and between each nearest neighbor pair of oxygen ions is a proton (H^+). Because of charge neutrality, two of the neighboring hydrogen ions are near their oxygen ion, and two are further away – this condition is called the ice rule or Bernal–Fowler rules [3]. In 1935, Pauling noted that the number of configurations W_N conforming to ice rule grows exponentially with the number of oxygen ions N [4]. He estimated $W_N \approx (3/2)^N$, leading to a residual entropy $S = k_B \cdot \ln W_N = k_B N \ln(3/2)$. Therefore we can define the zero-temperature entropy as an extensive quantity.

In 1956, Anderson proposed that the charge frustration in magnetite, given by the chemical formula $[Fe^{3+}]_A[Fe^{3+}Fe^{2+}]_BO_4$, leads to a ground state degeneracy that is also governed by the ice rule [5]. The subscript A denotes the tetrahedrally, and B the octahedrally coordinated lattice sites of AB_2O_4 the spinel. The ions on the B sites form a pyrochlore lattice, which is a lattice built from corner-shared tetrahedra. The charge frustration can be modeled by antiferromagnetically coupled Ising spins on a pyrochlore lattice. The Ising spins stand for the deviation from the charge neutrality. A further example is the recently discovered spin ice, where the role of the Ising spins is played by the anisotropic magnetic moments of the rare-earth ions forming the pyrochlore lattice [6].

In 2020, King *et al.*[1] realized a new type of artificial spin ice made by a radio-frequency superconducting flux qubits system. They checked the validity of the ice rule at finite temperatures and experimentally investigated magnetic monopole-like excitations. Their setup allows studying quantum phenomena, which encourages further research and potential applications. Here I present a minimal model, which introduces the basic features of their system.

1.2 Quantum six-vertex model and square lattice

The displacement of the H^+ ions from the center of the bonds in water ice can be represented by arrows emanating into and from the lattice points standing for the O^{2-} ions. The ice rule is equivalent to having six possible configurations of 2-in/2-out arrows. The ice rule expressed with such arrows is the six-vertex model.

The two-dimensional six-vertex model is called the square ice model. In 1967, Lieb found the exact solution of the residual entropy for the square ice $S = k_B N \ln(4/3)^{3/2}$ [7]. The six-vertex model can be extended by dynamics arising from quantum phenomena, and we get the so-called quantum six-vertex model (Q6VM). Here the quantum effect is manifested by a finite-amplitude flipping term in the Hamiltonian. This term reverses the arrows on a plaquette, where arrows are joined nose to tail. For the square lattice, this type of dynamics is shown in Fig. 1 in different types of representations (see Appendix A).

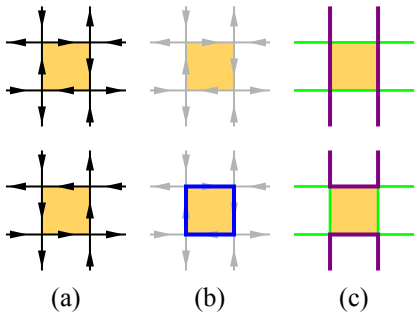

Figure 1: The act of the quantum flipping on a flippable plaquette of the square lattice (a) in the arrow representation, (b) in the flipping representation, and (c) in the fully packed loop representation.

In 2004, Shannon *et al.* [2] considered the frustrated Ising model on the checkerboard lattice, which can be mapped to the Q6VM on the square lattice. They used the following Hamiltonian to describe the system:

$$\begin{aligned}\mathcal{H}_{\text{Q6VM}} &= \mathcal{H}_t + \mathcal{H}_V, \\ \mathcal{H}_t &= -t \sum_{\text{plaquettes}} \Big(|\circlearrowleft\rangle\langle\circlearrowright| + |\circlearrowright\rangle\langle\circlearrowleft| \Big), \\ \mathcal{H}_V &= V \sum_{\text{plaquettes}} \Big(|\circlearrowleft\rangle\langle\circlearrowleft| + |\circlearrowright\rangle\langle\circlearrowright| \Big),\end{aligned} \tag{1}$$

where the sum is over the squares (plaquettes) of the lattice. Here $\mathcal{H}_t$ is an off-diagonal term presenting the quantum flipping of the arrows, and $\mathcal{H}_V$ is a diagonal term measuring the number of the flippable plaquettes.

They found three phases for different V/t ratios. For $V < V_c \approx -0.3437t$, we find the "totally flippable" states, where every plaquette in the lattice is flippable – for spin systems, it is named Neél phase. In contrast, the flippable plaquettes are suppressed for $V > t$. This will result in a phase consisting of isolated states, with no flippable plaquettes. These are exact eigenstates of the Hamiltonian (1) with 0 energy. The $V/t = 1$ realizes the quantum critical point of Rokhsar-Kivelson (RK point), where all classical configurations have the same amplitude in the ground state. For $V_c/t < V/t < 1$, there is a two-fold degenerate ground state as a consequence of the quantum flipping term, what we call the "plaquette phase".

The plaquette phase is a key concept in the Q6VM. The states of the plaquette phase contain flippable corner-shared plaquettes which resonate independently from each other, see Fig. 2. Hence we can distinguish two corresponding states, whose wave functions I denote by $|\Psi\rangle_{\text{AD}}$ and $|\Psi\rangle_{\text{BC}}$, as shown in the figure. The $|\Psi\rangle_{\text{AD}}$ can be approximated by the following variational wave function:

$$|\Psi\rangle_{\text{AD}} = \frac{1}{2} |\circlearrowleft + \circlearrowright\rangle_{\text{A}} |\circlearrowleft + \circlearrowright\rangle_{\text{D}} \ , \tag{2a}$$

$$|\Psi\rangle_{\text{BC}} = \frac{1}{2} |\circlearrowleft + \circlearrowright\rangle_{\text{B}} |\circlearrowleft + \circlearrowright\rangle_{\text{C}} \ , \tag{2b}$$

where $|\circlearrowleft + \circlearrowright\rangle_{\text{A}}$ represents the resonating flippable plaquettes in cells A, introducing a notation used throughout this paper.

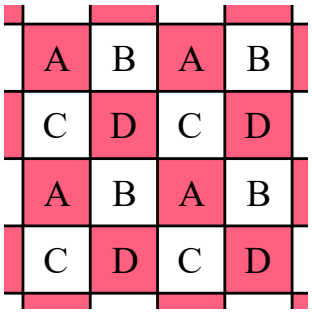

Figure 2: The square lattice can be divided into quadripartite cells. In the plaquette phase, the flippable states on the corner-shared plaquettes (e. g. A and D) resonate independently from each other. The two possible choices of the resonating plaquettes are highlighted with colors: A and D with pink, and B and C with white. Thus the plaquette phase has 2-fold degeneracy.

In my research, I apply an extended version of the Q6VM motivated the artificial spin ice of King *et al.* [1]. It turns out that distinguishing between the energy levels of the allowed vertex configurations affects the classical and quantum phase diagram significantly. The six possible vertex configurations of Q6VM can be divided into two types, as shown in Fig. 3. Let us denote the operator that measures whether a vertex belongs to Type I or to Type II by $|\kappa_{\mathrm{I}}\rangle\langle\kappa_{\mathrm{I}}|$ or $|\kappa_{\mathrm{II}}\rangle\langle\kappa_{\mathrm{II}}|$. If a Type I vertex has ε_{I} energy and a Type II vertex has $\varepsilon_{\mathrm{II}}$ energy, the energy difference is $J = \varepsilon_{\mathrm{II}} - \varepsilon_{\mathrm{I}}$. As a consequence, a new term ($\mathcal{H}_J$) appears in the effective Hamiltonian $\mathcal{H}$. I call this extended model the anisotropic quantum 6 vertex model, with the Hamiltonian

$$\begin{aligned} \mathcal{H} &= \mathcal{H}_V + \mathcal{H}_t + \mathcal{H}_J \ , \\ \mathcal{H}_J &= \sum_{\text{vertices}} J\,|\kappa_{\mathrm{II}}\rangle\langle\kappa_{\mathrm{II}}| \ . \end{aligned} \tag{3}$$

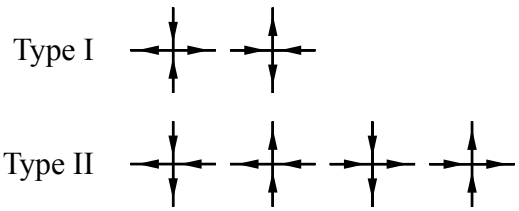

Figure 3: The two types of possible vertex-configurations in Q6VM.

2 Classical phase diagram

In this section, I will investigate the properties of the square lattice using analytical and numerical tools. In section 2.1, I prepare the finite size cluster to compute, define topological sectors and use them to classify the states. Following this, in section 2.2, I will construct the classical phase diagram and characterize its phases.

2.1 The construction and the topology of the lattice

I construct clusters with periodic boundary conditions generated by two lattice vectors, as shown with green arrows in Fig. 4(a) for the cluster made of 16 vertices. To characterize a cluster, I use its symmetries and its system size N. System size indicates the number of vertices, thus the system contains $2N$ spins represented by arrows. I generate the ice rule configurations starting from a reference state containing only flippable plaquettes, as shown in Fig. 4(a). It is easy to see that by flipping a (flippable) plaquette, or bonds along a random closed-loop built by interlocking arrows, we generate a new state that satisfies the ice rule. Therefore I implemented a random algorithm to find all or almost all possible six-vertex configurations of a given cluster. These configurations span the Hilbert space.

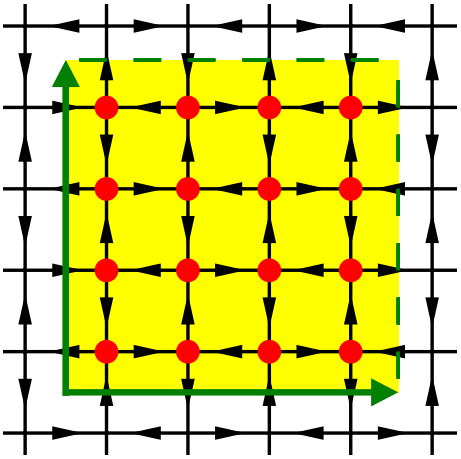

(a)

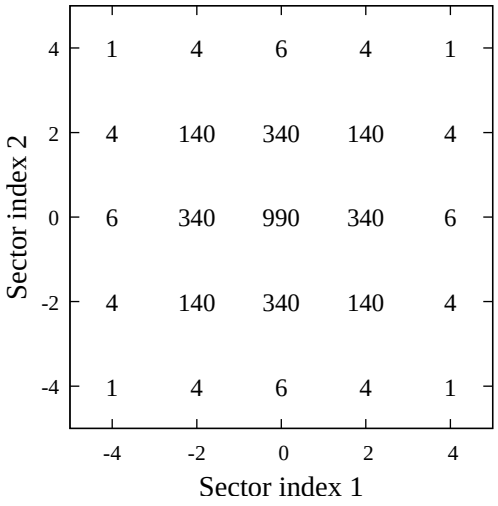

(b)

Figure 4: (a) A finite size cluster with periodic boundary conditions and system size $N = 16$, defined by green arrows. The vertices (sites) are shown by red points. All the plaquettes are flippable, this is the reference state used to construct the six-vertex configurations. In this case, the point group symmetries of the cluster are the same as of the original square lattice. (b) The number of states in each topological sector for this cluster.

The configurations can be divided into topological sectors. Two configurations are in the same topological sector if they can be transformed into each other only by flipping plaquettes. In general, for a cluster with periodic boundary conditions (isomorphic to a torus), topological sectors are described by two indices representing the signed sum

of the directed bonds crossing the two boundaries (or any horizontal and vertical line). The periodic condition and the ice rule guarantee the unique value of the indices. As an example, Fig. 4(b) presents the topological (sector) map of a 16-vertex system. A special property of the square lattice is that in the inner part of the topological map, all states with the same indices are connected by flipping plaquettes (they are in the same topological sector). Whereas, at the border, an index pair covers several sectors separated from each other. On this lattice, it is precisely the states without flippable plaquettes that form a sector alone – these are the isolated states.

2.2 Analytic description of the classical case

In the classical case corresponds to t=0, when the off-diagonal terms in the Hamiltonian are absent and only the diagonal terms remain,

$$\mathcal{H}_{\mathrm{Cl}} = \mathcal{H}_V + \mathcal{H}_J = \sum_{\text{plaquettes}} V\Big(|\circlearrowleft\rangle\langle\circlearrowleft| + |\circlearrowright\rangle\langle\circlearrowright|\Big) + \sum_{\text{vertices}} J\,|\kappa_{\mathrm{II}}\rangle\,\langle\kappa_{\mathrm{II}}|\ . \tag{4}$$

The energy of a state is determined only by the number of the flippable plaquettes (n_V) and the second-type vertices (n_J). Therefore, the energies of each state can be compared using only these two numbers for given values of V and J. For a finite system with periodic boundary conditions, the energy of a given state Φ is

$$E = \langle\Phi|\mathcal{H}_{\mathrm{Cl}}|\Phi\rangle = V n_V(\Phi) + J n_J(\Phi)\,. \tag{5}$$

Hence, to sketch the classical phase diagram it is enough to know the possible values of $(n_V(\Phi), n_J(\Phi))$ pairs. According to this, I noted three constraints – derived in Appendix B:

$$n_J \le N\ , \tag{6a}$$
$$2n_V + n_J \le 2N\ , \tag{6b}$$
$$N \le n_V + n_J\ , \tag{6c}$$

for a cluster formed by N vertices. The six-vertex states can be characterized by their $(n_V(\Phi), n_J(\Phi))$ pairs, as shown Fig. 5(a) for the cluster with system size N=16.

Based on these findings, I found 3 possible phases, and the classical phase diagram is presented in Fig. 5(b). One of these is the 2-fold degenerated totally flippable phase containing states that have only flippable plaquettes and Type I vertices ($n_V = N$, $n_J = 0$). The classical state can be written in the following form:

$$|\mathrm{TF1}\rangle = |\circlearrowleft\rangle_{\mathrm{A}}\,|\circlearrowleft\rangle_{\mathrm{D}} \equiv |\circlearrowright\rangle_{\mathrm{B}}\,|\circlearrowright\rangle_{\mathrm{C}}\ , \tag{7}$$
$$|\mathrm{TF2}\rangle = |\circlearrowright\rangle_{\mathrm{A}}\,|\circlearrowright\rangle_{\mathrm{D}} \equiv |\circlearrowleft\rangle_{\mathrm{B}}\,|\circlearrowleft\rangle_{\mathrm{C}}\ .$$

The remaining two phases contain only Type II vertices ($n_J = N$). The second one, called the square phase, maximizes the number of flippable plaquettes ($n_V = N/2$) and it is 4-fold degenerate. The third one is the isolated phase with non-flippable configurations ($n_V = 0$). It is a subextensive manifold.

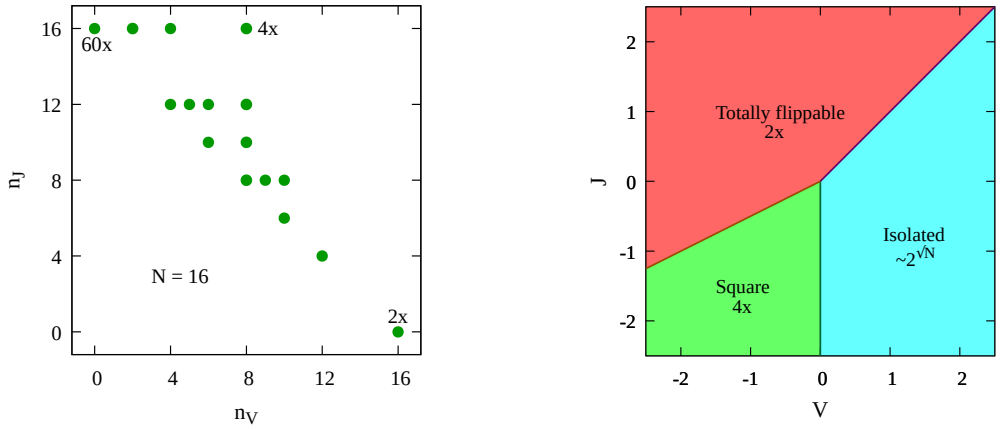

(a) (b)

Figure 5: (a) The possible (n_V, n_J) pairs for system size N=16. (b) The classical phase diagram of the square lattice. Every individual phase has a characteristic (n_V, n_J) value pair, structure, and degeneracy – the latter is shown on the diagram. The slope of the boundary line between the totally flippable and square phase is 1/2, between the totally flippable and isolated phase is 1.

Of these, the appearance of the square phase is new compared to previous findings. Its four classical states motivate the quadripartite decomposition of the square lattice, which can be used to establish a connection with the plaquette phase that will appear in the quantum case. The visual representation of these remarks is in Fig. 6. The wave functions of the four classical square states are

$$|\mathrm{SqA}\rangle = |\circlearrowleft\rangle_{\mathrm{A}} |\circlearrowright\rangle_{\mathrm{D}} \ , \tag{8a}$$
$$|\mathrm{SqD}\rangle = |\circlearrowright\rangle_{\mathrm{A}} |\circlearrowleft\rangle_{\mathrm{D}} \ , \tag{8b}$$
$$|\mathrm{SqB}\rangle = |\circlearrowleft\rangle_{\mathrm{B}} |\circlearrowright\rangle_{\mathrm{C}} \ , \tag{8c}$$
$$|\mathrm{SqC}\rangle = |\circlearrowright\rangle_{\mathrm{B}} |\circlearrowleft\rangle_{\mathrm{C}} \ , \tag{8d}$$

where the states are indexed by the counterclockwise oriented flippable plaquettes. Interestingly, in both the fully packed and flipping representations, the classical square states actually show up as squares.

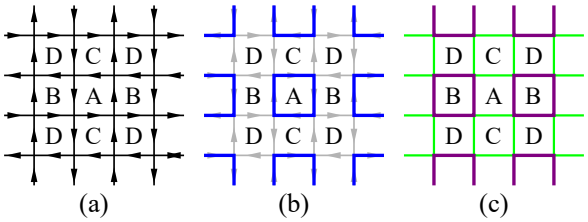

Figure 6: The classical square state $|\Psi\rangle_{\mathrm{Sq1}}$ in the quadripartite lattice (a) in the arrow representation, (b) in the flipping representation, and (c) in the fully packed loop representation.

3 Quantum phase diagram

Having constructed the classical phase diagram, we turn our attention to quantum effects with a finite value of t. I will apply different analytical and numerical methods to draw a $J/t - V/t$ diagram.

3.1 Symmetries and order parameters

To determine and describe the different phases in the quantum mechanical case, I shall find their order parameters and the symmetries that they break, characterizing the long-term order. To achieve this, I have to find out the symmetry properties of the lattice.

All of the known phases of the (0,0) topological sector (totally flippable, plaquette, and square) are compatible with the quadripartite decomposition of the lattice – they are invariant with respect to translations by $(2, 0)$ and $(0, 2)$ lattice vectors. Thus I have drawn the vertex configuration shown in Fig. 7, whose symmetries are the same as those of the finite periodic lattice and are also valid in the infinite limit.

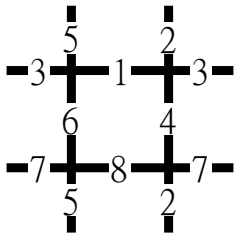

Figure 7: A four-site unit cell containing eight enumerated bonds.

The following four elementary transformations generate the symmetry group of the four-site cluster: a translation τ_x along the horizontal direction, a translation τ_y along the vertical direction, a 4-fold rotation C_4, and an reflection σ in the vertical plane. Using cyclic permutations they are written as

$$\sigma = (2, 5)(4, 6) \,, \tag{9a}$$

$$C_4 = (1, 4, 8, 6)(2, 7, 5, 3) \,, \tag{9b}$$

$$\tau_x = (1, 3)(2, 5)(4, 6)(7, 8) \,, \tag{9c}$$

$$\tau_y = (1, 8)(2, 4)(3, 7)(5, 6) \,. \tag{9d}$$

To investigate this problem, it is convenient to choose the *fully packed loop representation* (see Appendix A). In the reference state, the horizontal bonds are charged, the vertical ones are not. Here flipping a plaquette corresponds to rotating the position of the charged bonds by 90° – the uncharged bonds become charged and vice versa. It is shown in Fig. 1(c), where the purple color stands for charged bonds, the green color for uncharged bonds. The fully packed loop representation is closely related to the quantum dimer model of Rokhsar and Kivelson [8].

The advantage of this representation is that it converts the direction of a bond to a scalar quantity (charge) which is more easily treated to define order parameters. Consequently, I can interpret quantities in the four-site unit cell presented as functions of the charge of the bonds. The order parameters are also such quantities. From the unit cell, most of these can be generalized also to the finite, periodic lattice.

The irreducible representations of the symmetry group of the four-site unit cell can be used to identify the order parameters. After calculations, it turns out, there is an order parameter transforming as a one-dimensional, and three pairs transforming as a two-dimensional irreducible representation. Fig. 8 visually presents them.

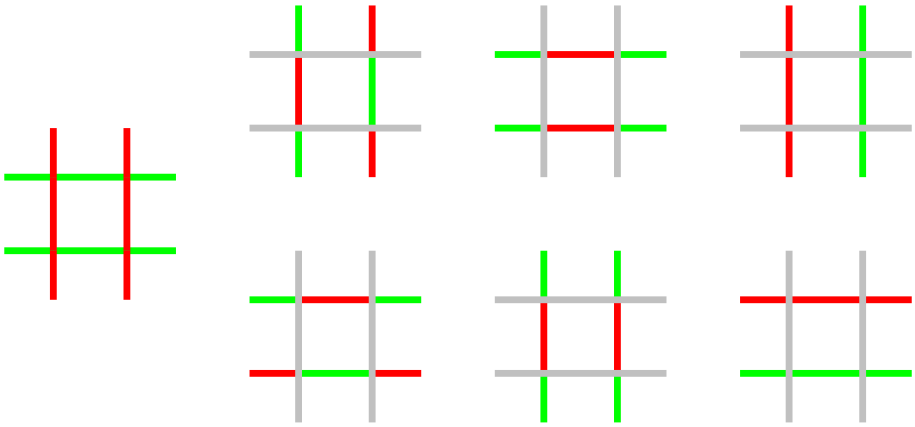

Figure 8: The non-zero order parameters of the system. The red and green colors measure the charge of the bonds with opposite signs. The weights on the grey bonds are 0.

These order parameters distinguish the totally flippable and the square phases. They can also be used to identify the order of the phase transitions. For this, we should construct the Landau free energy. This is under investigation, as I will mention in section 4.2.

Furthermore, we shall be careful when we extend the translation operator to the lattice in each representation. This is because, in the arrow and flipping representations, the translations of the arrows by unit lattice vectors result in the *conjugation* of the reference state, whereas in the fully packed loop representation the reference state is invariant under τ_x and τ_y. In the arrow and flipping representations, the *conjugation* $\mathcal{C}$ means we reverse the direction of all arrows. It is worth noting that $\mathcal{C}$ commutes with all generators of the symmetry group and the Hamiltonian. Furthermore, $\mathcal{C}^2$=1. In the fully packed loop representation, the $\mathcal{C}$ makes the uncharged bonds charged and vice versa. Therefore we define the operators $\mathcal{T}_\delta$ and $\widetilde{\mathcal{T}}_\delta$ of translation with $\delta = (\delta_x,\delta_y)$ for the arrow and the fully packed loop representation:

$$\mathcal{T}_\delta = \sum_{\text{Unit cells}} \tau_x^{\delta_x}\tau_y^{\delta_y}\mathcal{C} \ , \tag{10a}$$

$$\widetilde{\mathcal{T}}_\delta = \sum_{\text{Unit cells}} \tau_x^{\delta_x}\tau_y^{\delta_y} \ . \tag{10b}$$

These operators leave the reference state unchanged in both representations, to ensure the consistency of the used representations. Consequently, let us see how the classical

states of the totally flippable and the square phases transform under the elementary translations in the arrow or flipping representation:

$$\mathcal{T}_{(1,0)}\,|\mathrm{TF1}\rangle = \mathcal{T}_{(0,1)}\,|\mathrm{TF1}\rangle = |\mathrm{TF1}\rangle \ , \tag{11a}$$
$$\mathcal{T}_{(1,0)}\,|\mathrm{TF2}\rangle = \mathcal{T}_{(0,1)}\,|\mathrm{TF2}\rangle = |\mathrm{TF2}\rangle \ , \tag{11b}$$
$$\mathcal{T}_{(1,0)}\,|\mathrm{SqA}\rangle = |\mathrm{SqB}\rangle\,, \quad \mathcal{T}_{(0,1)}\,|\mathrm{SqA}\rangle = |\mathrm{SqC}\rangle \ , \tag{11c}$$
$$\mathcal{T}_{(1,0)}\,|\mathrm{SqB}\rangle = |\mathrm{SqA}\rangle\,, \quad \mathcal{T}_{(0,1)}\,|\mathrm{SqB}\rangle = |\mathrm{SqD}\rangle \ , \tag{11d}$$
$$\mathcal{T}_{(1,0)}\,|\mathrm{SqC}\rangle = |\mathrm{SqD}\rangle\,, \quad \mathcal{T}_{(0,1)}\,|\mathrm{SqC}\rangle = |\mathrm{SqA}\rangle \ , \tag{11e}$$
$$\mathcal{T}_{(1,0)}\,|\mathrm{SqD}\rangle = |\mathrm{SqC}\rangle\,, \quad \mathcal{T}_{(0,1)}\,|\mathrm{SqD}\rangle = |\mathrm{SqB}\rangle \ . \tag{11f}$$

3.2 A simple phase diagram by a variational method

Based on the previous results and the classical phase diagram, there are at least four phases (totally flippable, square, isolated, and plaquette) that should appear in the quantum phase diagram. I will sketch a variational phase diagram by comparing the expectation values of the Hamiltonian for the wave function of different phases.

For the totally flippable, the square, and the isolated classical states $\langle\Psi|\mathcal{H}_t|\Psi\rangle = 0$, because $\mathcal{H}_t$ contains only off-diagonal terms. Their energies are the same as in the classical limit, see equation (5). In the case of the plaquette phase, I should calculate probabilities to determine the expected value of the number of the flippable plaquettes and the Type II vertices, derived in the following ($|\Psi_{\mathrm{Plaq}}\rangle$ is one of wave functions from equation (2)):

$$E_{\mathrm{Plaq}} = \langle\Psi_{\mathrm{Plaq}}|\mathcal{H}|\Psi_{\mathrm{Plaq}}\rangle = \langle\Psi_{\mathrm{Plaq}}|\mathcal{H}_V|\Psi_{\mathrm{Plaq}}\rangle + \langle\Psi_{\mathrm{Plaq}}|\mathcal{H}_J|\Psi_{\mathrm{Plaq}}\rangle + \langle\Psi_{\mathrm{Plaq}}|\mathcal{H}_t|\Psi_{\mathrm{Plaq}}\rangle \ ,$$
$$E_{\mathrm{Plaq}} = \left(\frac{N}{2} + \frac{N}{2}\times\frac{2}{2^4}\right)V + \frac{2}{2^2}\times NJ - \frac{N}{2}\times t = N\times\left(\frac{9V}{16} + \frac{J}{2} - \frac{t}{2}\right) \ . \tag{12}$$

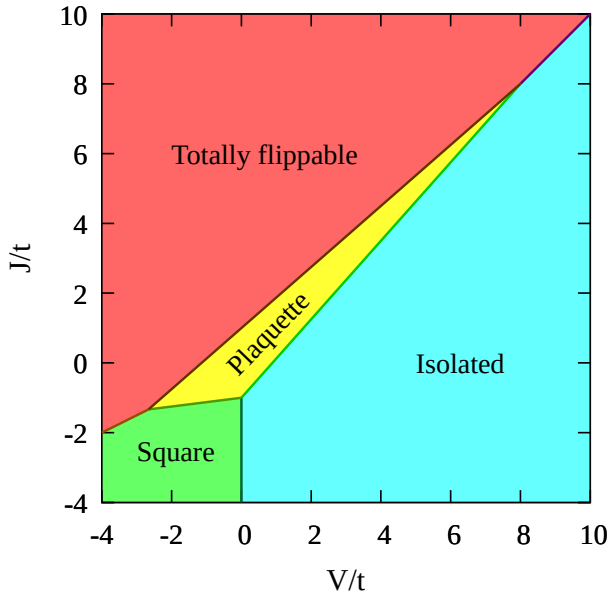

Figure 9: The quantum phase diagram of the variational approximation.

Comparing the energies I can identify the phase of the ground state at every point. Hence, I get an approximate phase diagram in Fig. 9.

This simple variational approximation fails to reproduce the precise phase boundaries on the isotropic ($J/t = 0$) line: the boundary between the plaquette and isolated phase is at $V/t = 8/9$, instead of the exact $V/t = 1$ (the Rokhsar-Kivelson point) [2]. It is the consequence of the variational approximation overestimating the energy of the plaquette phases. In addition, each isolated state is an exact eigenstate of the Hamiltonian with energy $E_{\mathrm{Iso}} = NJ$. Hence this particular boundary point is larger than $V/t = 8/9$, reconciling with the previous works.

3.3 Ground states and phase boundaries with exact diagonalization

Based on the discussion above, we may assume that the totally flippable, square and plaquette phases appear in the quantum phase diagram, but do they exhaust all the possibilities? And what are the precise transitions between them? To characterize and localize these phase boundaries I use two methods. The first one is the numerically exact diagonalization (ED) for finite clusters with the Lánczos method. This will provide the energies of the ground and low-lying excited states. The second one is the comparison of the ground state energies obtained from fourth-order perturbation theory, detailed in section 3.4.

Firstly, I checked for the smaller system size $N = 16$ to which topological sectors the ground states belong. The classical states of the totally flippable, square phases and the plaquette phases are in the topological sector (0,0), while for the isolated states at least one of their topological indices must be extremal. From the variational approximation, we expect to see only these two types of topological sectors. The results are surprisingly different because other sectors also appeared in the diagram at the boundary between the totally flippable and the isolated phase, as is shown in Fig. 10. For bigger system sizes (N=20, 32, 36), I obtained similar results. Their origin is currently under investigation, as will be mentioned in section 4.2. In this paper, I will not deal with this part of the phase diagram.

Knowing the symmetry properties of the classical states of the totally flippable and square phases, we can construct states that transform according to the irreducible representations of the translation group, using equations (7) and (8):

$$|\mathrm{TF}(0{,}0)_{\mathrm{e}}\rangle = |\mathrm{TF1}\rangle + |\mathrm{TF2}\rangle \ , \tag{13a}$$

$$|\mathrm{TF}(\pi,\pi)_{\mathrm{o}}\rangle = |\mathrm{TF1}\rangle - |\mathrm{TF2}\rangle \ , \tag{13b}$$

$$|\mathrm{Sq}(0{,}0)_{\mathrm{e}}\rangle = |\mathrm{SqA}\rangle + |\mathrm{SqD}\rangle + |\mathrm{SqB}\rangle + |\mathrm{SqC}\rangle \ , \tag{13c}$$

$$|\mathrm{Sq}(\pi{,}\pi)_{\mathrm{e}}\rangle = |\mathrm{SqA}\rangle + |\mathrm{SqD}\rangle - |\mathrm{SqB}\rangle - |\mathrm{SqC}\rangle \ , \tag{13d}$$

$$|\mathrm{Sq}(\pi{,}0)_{\mathrm{o}}\rangle = |\mathrm{SqA}\rangle - |\mathrm{SqD}\rangle - |\mathrm{SqB}\rangle + |\mathrm{SqC}\rangle \ , \tag{13e}$$

$$|\mathrm{Sq}(0{,}\pi)_{\mathrm{o}}\rangle = |\mathrm{SqA}\rangle - |\mathrm{SqD}\rangle + |\mathrm{SqB}\rangle - |\mathrm{SqC}\rangle \ . \tag{13f}$$

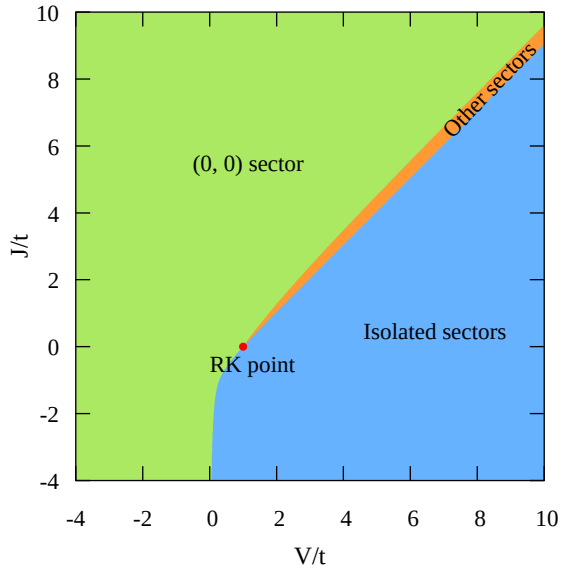

Figure 10: The topological sectors of the ground states in the quantum phase diagram, with system size N=16. Started from the Rokhsar-Kivelson point other unexpected sectors appear in the phase diagram.

They are at the k=(0,0), $(\pi,0)$, $(0,\pi)$, and (π,π) points in the Brillouin zone. The subscripts e and o denote whether the wave functions are even or odd under the application of conjugation $\mathcal{C}$. Using exact diagonalization for several system sizes (N=16, 20, 26, 32), I check that these states indeed appear in the ground states of the totally flippable and square phases.

The Lánczos method is an iterative procedure that calculates a spectrum starting from an initial state by applying the Hamiltonian successively. It preserves the symmetry, i. e. the momentum of the state in the Brillouin zone, of the initial state, or in other words, does not leave the *symmetry sector*. As a result, we obtain the ground and low-lying excited states in the symmetry sector determined by the initial state. Therefore I initialized the Lánczos method from the states given by equation (13). Fig. 11 presents results for a system N=32.

There are several things I need to clarify or at least note about the results. The first one is the energy levels of $|\mathrm{Sq}(\pi,0)_\mathrm{o}\rangle$ and $|\mathrm{Sq}(0,\pi)_\mathrm{o}\rangle$ are the same with high precision. Since these belong to the same irreducible representation of the space group $(D_4 \times T)$, this result is as expected.

The second one is related to the states at the momentum (π,π) of the Brillouin zone. Here the spectra of the Lánczos ED starting from $|\mathrm{TF}(\pi,\pi)_\mathrm{o}\rangle$ and $|\mathrm{Sq}(\pi,\pi)_\mathrm{e}\rangle$ were distinct. Its reason is that they have different symmetry properties, namely respect to the conjugation $\mathcal{C}$, preserved by the Lánczos method.

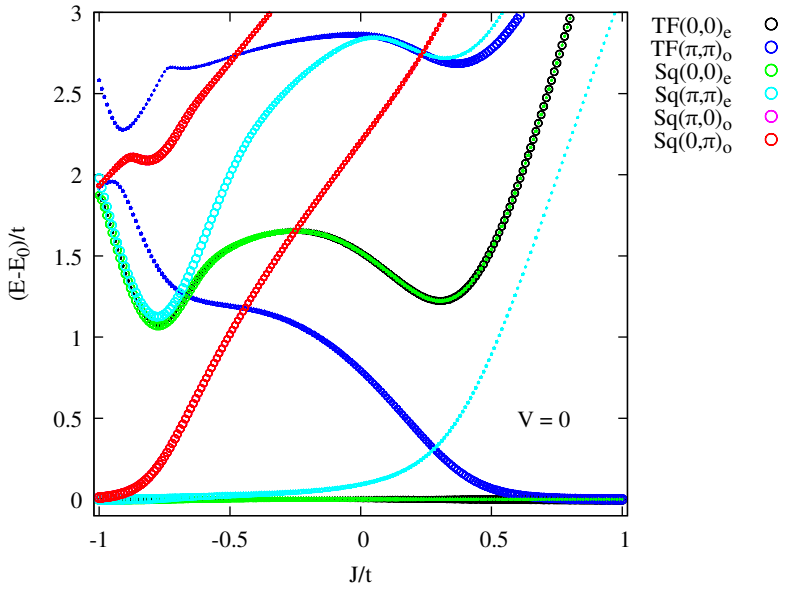

Figure 11: The energy levels in different symmetry sectors for a cluster with system size N=32. The circles are labeled by the initial wave functions defined by equations (13), and the radii of the circles denote their overlap with the particular state.

For large negative values of V/t, we recognize four low-lying states separated by a gap from the rest of the spectrum. These belong to the square phases, which split because of the finite size of the system. As V/t approaches zero, the two odd states are separated by an increasing gap from the two even states. These two even states make the plaquette phase [2]. Therefore it is a suitable approximation to consider the crossing point of the levels of $|\mathrm{TF}(\pi,\pi)_\mathrm{o}\rangle$ and $|\mathrm{Sq}(\pi,0)_\mathrm{o}\rangle$ (or $|\mathrm{Sq}(0,\pi)_\mathrm{o}\rangle$) as the boundary between the square and plaquette phases.

Similar observations can be made for the large positive values of V/t, where there are two finite-size split states of the totally flippable phase. Here the crossing point of the levels of $|\mathrm{TF}(\pi,\pi)_\mathrm{o}\rangle$ and $|\mathrm{Sq}(\pi,\pi)_\mathrm{e}\rangle$ is the boundary between the totally flippable and plaquette phases. We note that for all three phases in the (0,0) topological sector the ground state has the same momentum $(\pi,\pi)_\mathrm{e}$.

In my experience, this method worked well only over a certain range. For values of V/t below the point where all three phases of the topological $(0,0)$ sector meet, the order of levels changed and the spectrum looked different. Therefore it was difficult to identify the phase boundary between the totally flippable and square phases from the data. For $0.37 < V/t < 1$ and negative values of J/t, the appearance of the isolated phase makes the search for the crossing of the levels of $|\mathrm{Sq}(\pi,0)_\mathrm{o}\rangle$ and $|\mathrm{TF}(\pi,\pi)_\mathrm{o}\rangle$ meaningless. Furthermore, we should take care for the appearance of the other (unexpected) topological sectors for $J/t > 0$ and $V/t > 1$. Hence I investigated only in the range $V/t \leq 1$.

In the end, this allowed to meaningfully define parts of the upper and lower boundaries of the plaquette phase. The calculations were mainly performed for a system size of N=32. At some points, I repeated the procedure for N=16,20,26,36 system sizes to perform finite-size scaling – a procedure that has been successfully applied in the isotropic limit case [2]. However, the results showed that the finite-size scaling is not well defined.

As a next step, we focus on the boundary of the isolated phases for $J/t \leq 0$. The problem here is much simpler than in the (0,0) topological sector because the ground state energy of the isolated states is exactly $E_{\text{Iso}} = NJ$ (see the discussion of the equation (5)). Comparing this value with the numerically calculated ground state energy (using ED on the Hamiltonian) I read off the boundaries. As a check, I can simply calculate the eigenfunction of the ground state to see whether it really contains only the classical isolated states.

Finally, I could draw a phase diagram for $-1.75 < V < 1$ using exact diagonalization. The result is shown in Fig. 12.

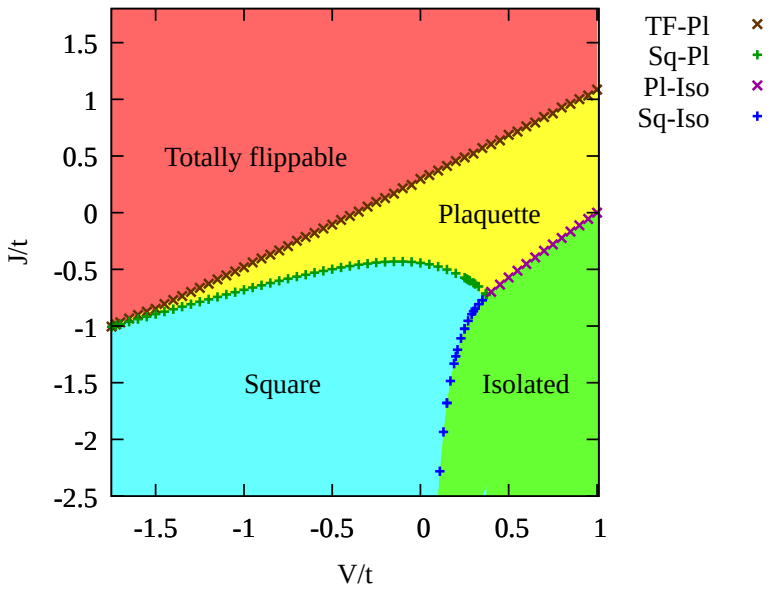

Figure 12: The explored phase diagram for system size N=32 with exact diagonalization.

3.4 Phase boundaries from perturbation theory

In this section, I approach the problem of finding the phase boundary by using fourth-order perturbation theory in $\mathcal{H}_t$ analytically. I calculated the energy corrections of the ground state for the square and totally flippable phases. Comparing these two energies we obtain the first-order boundary between the corresponding phases. Similarly, we may get the boundary between the isolated states and the squares phases as well (in this case, the ground state energy of the isolated states is known exactly). The textbook of *Messiah* gives [9] the nth order correction of the ground state energy:

$$\varepsilon^{(n)} = \text{Tr} \sum_{k_1,k_2,\ldots k_{n+1}=0}^{(n-1)} g^{k_1} V g^{k_2} V .. V g^{k_{n+1}} \ , \tag{14}$$

where V is the perturbation operator (here V=$\mathcal{H}_t$) and g is an operator defined by the ground state wave function $|0\rangle$, ground state energy E_0, unperturbed Hamiltonian H_0

(now $H_0 = \mathcal{H}_{\mathrm{Cl}}$) and its orthonormal basis $\{\varphi\}$:

$$g^k = \begin{cases} -|0\rangle\langle 0| & k = 0\ , \\ \sum_{\varphi\neq|0\rangle} \dfrac{1-|0\rangle\langle 0|}{(E_0 - \langle\varphi|H_0|\varphi\rangle)^k} & k \geq 0\ . \end{cases} \tag{15}$$

Since $\mathcal{H}_{\mathrm{Cl}}$ is diagonal for the classical states, the calculation of the perturbation series is straightforward for the square and totally flippable phases. Let us choose $|0\rangle$ as one of the classical states given in equations (7) and (8). It is easy to see that the first- and third-order corrections vanish, and we are left with the following formulas for the second and fourth orders corrections (see Appendix C):

$$\varepsilon^{(2)} = \sum_X \frac{1}{E_0 - E_X} \langle 0|\mathcal{H}_t|X\rangle\langle X|\mathcal{H}_t|0\rangle\ , \tag{16}$$

$$\begin{aligned}\varepsilon^{(4)} =& \sum_X \sum_{Y_X} \frac{1}{(E_0 - E_X)^2(E_0 - E_{Y_X})} \langle 0|\mathcal{H}_t|X\rangle\langle X|\mathcal{H}_t|Y_X\rangle\langle Y_X|\mathcal{H}_t|X\rangle\langle X|\mathcal{H}_t|0\rangle \\ &- \left(\sum_X \frac{1}{(E_0 - E_X)^2} \langle 0|\mathcal{H}_t|X\rangle\langle X|\mathcal{H}_t|0\rangle\right)\left(\sum_X \frac{1}{E_0 - E_X} \langle 0|\mathcal{H}_t|X\rangle\langle X|\mathcal{H}_t|0\rangle\right)\end{aligned} \tag{17}$$

where $|X\rangle$ is a classical state available by a single flip from the classical ground state $|0\rangle$, $|Y_X\rangle \neq |0\rangle$ is also a classical state available by the flipping of only one plaquette from $|X\rangle$.

Let us start with the case of the totally flippable phase. I illustrated the possible $|X\rangle$ and $|Y_X\rangle$ states in Fig. 13. From the equations above, we obtain the following corrections to the energy:

$$\begin{aligned}\varepsilon^{(2)}_{\mathrm{TF}} &= \frac{Nt^2}{4(V-J)}\ , \\ \varepsilon^{(4)}_{\mathrm{TF}} &= \frac{Nt^2}{16(V-J)^2}\left[\frac{4\times 2}{6(V-J)}t^2 + \frac{4\times 2}{7V-8J}t^2 + \frac{(N-13)\times 2}{8(V-J)}t^2\right] \\ &\quad - \frac{Nt^2}{16(V-J)^2}\frac{Nt^2}{4(V-J)} = \frac{Nt^4}{16(V-J)^2}\left[\frac{8}{7V-8J} - \frac{23}{12(V-J)}\right]\ .\end{aligned}$$

Similarly, I can repeat the same steps for the square phase. The possible $|X\rangle$ and $|Y_X\rangle$ states is shown in Fig. 14, and its corrections are

$$\begin{aligned}\varepsilon^{(2)}_{\mathrm{Sq}} &= \frac{N}{2}\times\frac{1}{4J}t^2 = \frac{Nt^2}{8J}\ , \\ \varepsilon^{(4)}_{\mathrm{Sq}} &= \frac{N}{2}\times\frac{t^2}{16J}\left[\frac{4\times 2}{8J-V}t^2 + \frac{4\times 2}{6J}t^2 + \frac{(N/2-9)\times 2}{8J}t^2\right] \\ &\quad - \left(\frac{N}{2}\right)^2\times\frac{t^2}{16J^2}\times\frac{t^2}{4J} = \frac{Nt^4}{16J^2}\left[\frac{4}{8J-V} - \frac{11}{24J}\right]\ .\end{aligned}$$

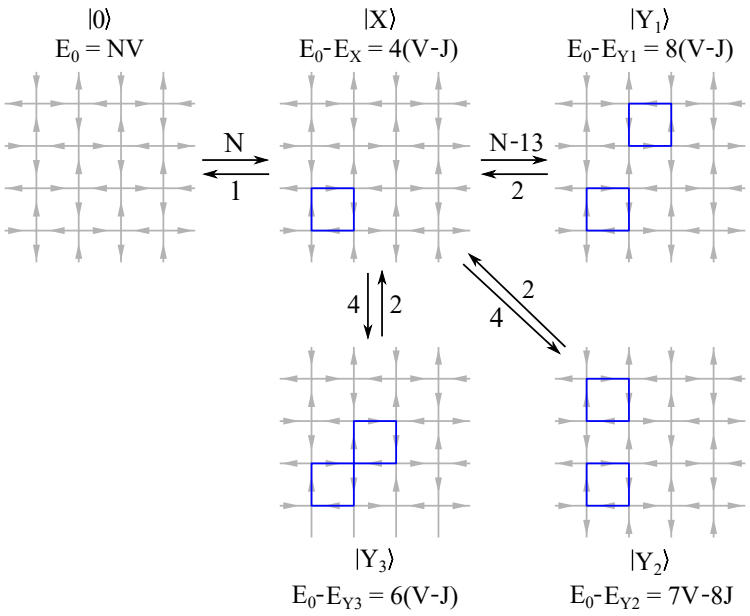

Figure 13: The excited states $|X\rangle$ and $|Y_X\rangle$ appearing in the equation (17) for the fourth-order correction of the ground state energy of the totally flippable phase. I noted the ground state energy (E_0), the excitation energies of the different states, and the number of possible transitions between them.

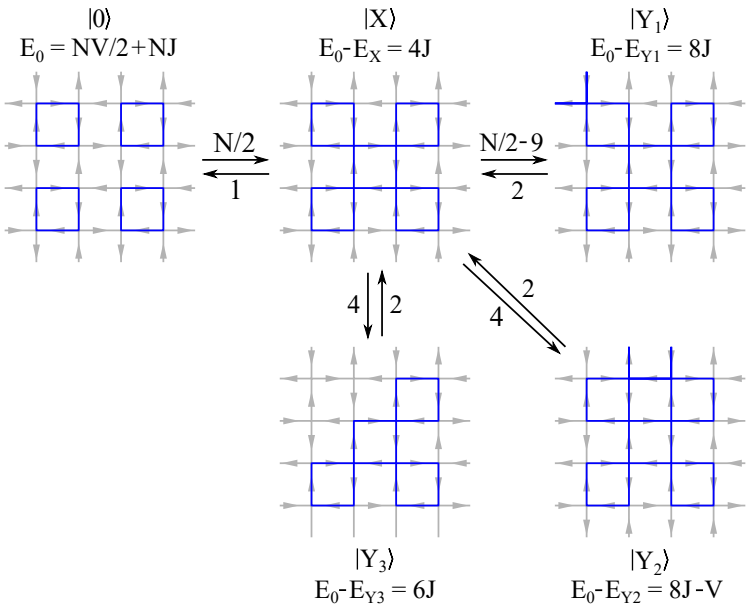

Figure 14: The excited states $|X\rangle$ and $|Y_X\rangle$ appearing in the equation (17) for the fourth-order correction of the ground state energy of the square phase. I noted the ground state energy (E_0), the excitation energies of the different states, and the number of possible transitions between them.

The ground state energies up to the fourth-order in the flipping amplitude t are

$$E_{\mathrm{TF}}^{(4)} = NV + \varepsilon_{\mathrm{TF}}^{(2)} + \varepsilon_{\mathrm{TF}}^{(4)} \,, \tag{20}$$

$$E_{\mathrm{Sq}}^{(4)} = \frac{NV}{2} + NJ + \varepsilon_{\mathrm{Sq}}^{(2)} + \varepsilon_{\mathrm{Sq}}^{(4)} \,. \tag{21}$$

Solving $E_{\mathrm{TF}}^{(4)} = E_{\mathrm{Sq}}^{(4)}$ we can draw the phase boundary between the corresponding phases. Its analytic form is

$$J = \frac{V}{2} + \frac{t^2}{4V} + \frac{t^4}{48V^3} + \mathcal{O}(t^6) \,. \tag{22}$$

Similarly, with $E_{\mathrm{Iso}} = E_{\mathrm{Sq}}^{(4)}$ the phase boundary of the square and the isolated phases is

$$V = -\frac{t^2}{4J} + \frac{t^4}{192J^3} + \mathcal{O}(t^6) \,. \tag{23}$$

I plotted these curves in Fig. 15 together with their Padé approximants and with the numerical results of the ED calculation. The Padé approximants allow estimating the convergence of the perturbation series. The results are reinforcing each other: the curves meet at two triple points to two decimal places. It is worth noting that the boundaries of the isolated and square phases from the ED and the fourth-order perturbation agree to two decimal places.

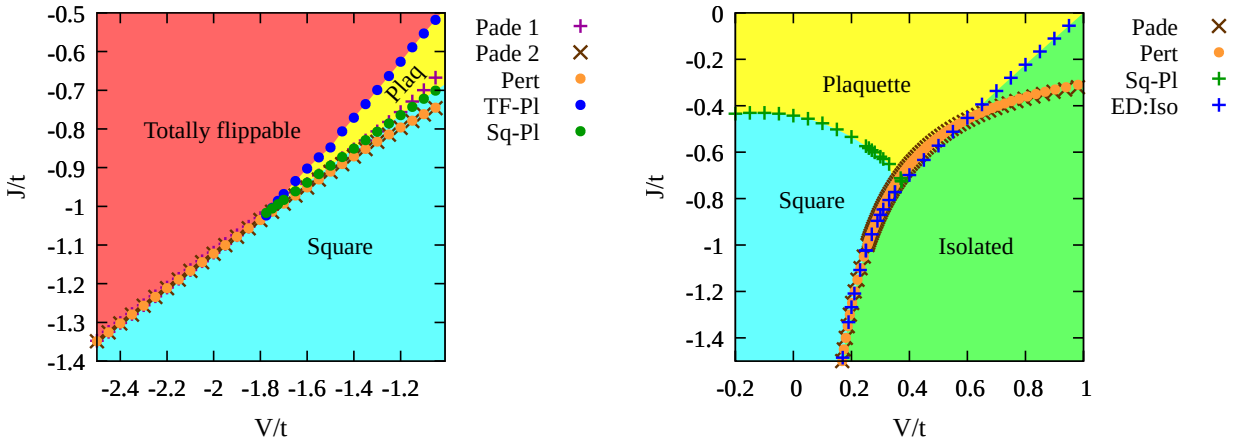

(a) (b)

Figure 15: Comparing the phase boundaries calculated by ED and fourth-order perturbation. We show the direct perturbational series together with their Padé approximants to estimate the convergence of the series. (a) The perturbational curve gives the boundary between the totally flippable and the square phases. It meets the lines (TF-Pl and Sq-Pl) from the ED at triple point $V/t \approx -1.75$ and $J/t \approx -1.01$. The Padé approximants do not deviate significantly in the relevant range. (b) The perturbational curve shows the boundary of the square and the isolated phases and the results of the ED near to the triple point $V/t \approx 0.37$ and $J/t \approx -0.72$. For $V/t < 0.37$, the results of the ED and the perturbational approach are the same to two decimal places.

4 Summary

4.1 Interpretation of the results

First, I focused on the classical case, where I identified the classical states that will be important later on, introduced their topological properties, and defined the classical states. I studied the problem computationally by generating finite-size clusters with periodic boundary conditions and system sizes N=16,20,26,32 and 36.

After that, I used a simple variational approximation to sketch a quantum phase diagram for $t \neq 0$. I found four different phases which can be characterized by their symmetries, topological sectors, and degeneracy of the ground state manifold – Tab. 1 summarizes the two last properties.

Phase name	Ground state degeneracy	Topological sector(s)
Totally flippable	2	(0,0)
Plaquette	2	(0,0)
Square	4	(0,0)
Isolated	$\sim 2^{\sqrt{N}}$	Sectors with extremal indices

Table 1: The basic properties of the explored phases.

For system size N=16 I checked whether other phases or sectors appear in the phase diagram or not. It turned out that the variational approach gives a qualitatively correct picture, except for the range enclosed by lines $V/t > 1$ and $J/t > 0$, where other topological sectors appear as a ground state (see Fig. 10). In this paper, I did not consider this part of the phase diagram.

To determine the phase boundaries approximately, I used exact diagonalization with the Lánczos method for a cluster with system size N=32 and calculated the fourth-order energy corrections of the phases analytically by perturbation theory. The different approaches nicely agreed. The different parts of the explored phase diagram are shown by Fig. 12 and 15.

4.2 Open questions

Many questions remain open in this model. One of the interesting questions is the order of the phase transitions. We hope to get an answer by constructing Landau free energy following the symmetry classification of the phases and order parameters. This would be particularly important for the plaquette phase boundaries. Furthermore, the order parameters may help in numerical calculations as well. It seems that one of these quantities is proportional to the number of Type II vertices n_J, and can be used to effectively determine the boundary between square and totally flippable phases. The preliminary results were in agreement with the fourth-order perturbation calculation to several decimal places. In the near future, we hope to be able to develop the theory in more detail and to perform further more accurate calculations.

Another promising idea is to refine the variational Ansatz we used. The variational wave function of the plaquette phase (see equation 2) can be generalized as the following forms:

$$|\Psi'(q)\rangle_{\mathrm{AD}} = \frac{1}{2+2q^2} \left|(1+q)\circlearrowleft + (1-q)\circlearrowright\right\rangle_{\mathrm{A}} \left|(1+q)\circlearrowleft + (1-q)\circlearrowright\right\rangle_{\mathrm{D}} \ , \tag{24a}$$

$$|\Psi''(p)\rangle_{\mathrm{AD}} = \frac{1}{2+2p^2} \left|(1+p)\circlearrowleft + (1-p)\circlearrowright\right\rangle_{\mathrm{A}} \left|(1-p)\circlearrowleft + (1+p)\circlearrowright\right\rangle_{\mathrm{D}} \ , \tag{24b}$$

It is easy to see that for q=p=0 these expressions give back $|\Psi\rangle_{\mathrm{AD}}$. For q=1, we get as a result $|\Psi'(1)\rangle$=$|\mathrm{TF1}\rangle$, and for q=−1 $|\Psi'(-1)\rangle$=$|\mathrm{TF2}\rangle$ – this suggest that the parameter q proportional to the order parameter of the totally flippable phase. Similarly, since $|\Psi''(1)\rangle$=$|\mathrm{SqA}\rangle$ and $|\Psi''(-1)\rangle$=$|\mathrm{SqD}\rangle$, the parameter p is connected to the order parameter of the square phase. As a result, we can determine the phase boundaries of the phase in the (0,0) topological sector more precisely. In addition, expanding the expectation value of the Hamiltonian in q and p will provide us with hints about the order of the phase transitions.

We can also design a wave function

$$|\Phi(r)\rangle = \frac{1}{\sqrt{2+2r^2}} \left|\circlearrowleft\right\rangle_{\mathrm{A}} \left|(1-r)\circlearrowleft + (1+r)\circlearrowright\right\rangle_{\mathrm{D}} \ . \tag{25}$$

which interpolates between the wave functions of the totally flippable and the square phases, $|\Phi(0)\rangle = |\mathrm{TF1}\rangle$ and $|\Phi(1)\rangle = |\mathrm{SqA}\rangle$. This can be a third way to determine this boundary.

As a next step, we shall understand how the totally flippable phase turns into the isolated phase in the range $V/t > 1$ and $J/t > 0$. The problem is caused by the emergence of new topological sectors whose symmetries have not yet been identified and whose ground state wave functions have not yet been identified analytically. While this is a tractable problem numerically, it is highly desirable to construct a theory for this transition. The classical states on the line $n_V + n_J$=N in Fig. 5(a) could be a suitable starting point for further theoretical investigations. It is conceivable that the quantum term and the numerical investigations on finite-size clusters cause the energy levels of these states to split the classical degeneracy at the phase boundary.

Finally, we shall calculate the dynamical structure factor and describe the possible excitations. The dynamical structure factor could help to compare our results with experimental findings at low temperatures. However, to access higher temperatures we should extend our model with states showing magnetic monopole-like behavior, because these do not obey the ice rule.

Acknowledgements

I would like to thank *Wigner Research Centre for Physics* for providing working conditions and financial support within their internship program. The calculations were run on a computer cluster financed in part by the NKFIH OTKA Grant No. K 124176.

I would particularly like to thank my supervisor, *Karlo Penc*, who has given me a lot of support and help, both professionally and personally, throughout our common work. I thank my friend *Levente Zsolt Nagy* for his advice on general computational questions at the beginning of my research.

The determination of the order parameters from irreducible representations and Fig. 1, 7, and 8 were done by my supervisor. The other parts of the thesis are all from my own work, including performing the calculations, developing algorithms and codes for the computational parts, determining the numerical results, drawing the phase diagrams and other figures.

A Representations of quantum 6-vertex model

There are many possibilities to represent a classical state in six-vertex models. Here I summarize four representations that are common in the literature.

Arrow representation: Here we show the direction of the bonds between vertices, just like the displacement vectors of the H^+ ions in the water spin ice.

Flipping representation: Similar to the notation of Baxter's textbook [10], I have arbitrarily chosen a totally flippable state as a reference, and I have colored gray or blue a bond depending on whether it is still the same as in the reference or not. In Fig. 16, the grey background shows the reference state.

Fully packed loop representation: It is connected to Anderson's paper on charge frustration in magnetite [5]. A loop segment represents a charge. Here a plaquette is flippable if its two opposite sides are colored, or in other words, charged. Its dynamic is that a flippable plaquette rotates by 90°, as it was shown in Fig. 1. A remarkable fact is the colored bonds must form continuous loops in the quantum six-vertex model. This representation is related to the quantum dimer models.

Height representation: The ice rule implies that the divergence of a vertex vanishes. Therefore we can arbitrarily choose a plaquette as a reference "height", and decrease or increase the height of the plaquettes around it by one, depending on the direction of the arrow between them.

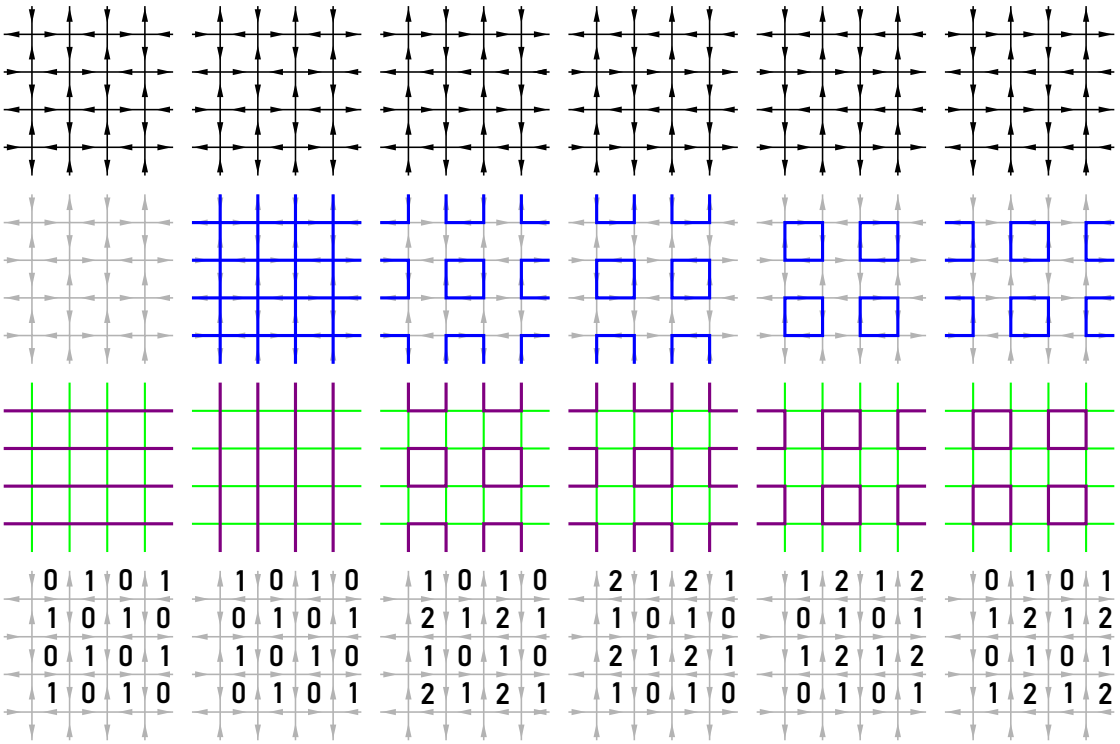

Figure 16: The representations of the totally flippable (first 2 columns) and square states (last 4 columns). Row-by-row they are the arrow, the flipping, the fully packed loop, and the height representation.

B Geometrical constraints of the classical states

The number of possible configurations in the ice rule manifold (W) grows exponentially with the system size (N). These configurations are identified as the classical states and thus form the basis of the Hilbert space. In table 2, I collect the size of the (0,0) topological sector ($W_{(0,0)}$) and the possible six-vertex configurations for the used clusters.

N	$W_{(0,0)}$	W
16	990	2970
20	5416	16248
26	73036	219108
32	962734	2891562
36	5482716	16448400

Table 2: The size of the (0,0) topological sector ($W_{(0,0)}$) and the Hilbert space for a cluster with system size N.

To calculate the energy of the classical states, we shall count the number of the flippable vertices (n_V) and the Type II vertices (n_J) (see equation (5)). Here too, the ice rule restricts the available (n_V, n_J) pairs. For these, I have made the following observations:

1. The maximum number of n_J is N, this is equation (6a). It is easy to see that if all of the horizontal or vertical lines in the lattice are directed nose to tail, all vertices are Type II, i. e. the isolated and the square states. Therefore, this estimation is sharp.

2. Out of the four plaquettes around a Type II vertex, at most two are flippable (see Fig. 3). Since each plaquette contains four vertices, for fixed value of n_J, in the most optimal case the number of flippable plaquettes $n_V \leq N - 2n_J/4$. It leads to equation (6b).

3. There is no other configuration on the line $2n_V+n_J = 2N$ connecting the square and the totally flippable states besides them. Reaching equality implies if a plaquette contains a Type II vertex, all of its vertices must be Type II. Therefore I fix a flippable plaquette with Type II vertices then it generates the whole lattice. Thank to the periodic boundary conditions, it is possible with proper layout, and they are called square states. In other cases there would be such states which would have less than four Type II vertices, thus they cannot satisfy the equality.

4. For a significant fraction of the ice-rule obeying states the equation $n_V + n_J{=}N$ holds – these states show up on the line defining the lower boundary of the "triangle" in the Fig. 5(a). I have not been able to construct a state, even by computer, for which this sum would have been less than N. Although I have not found an exact proof, I write the equation (6c) as an empirical constraint.

C Detailed calculations for the fourth order perturbation

In this section, I will derive for the special cases of the totally flippable and the square phases that the first- and third-order corrections vanish, and the second- and fourth-order corrections can be written in the forms of equations (16) and (17).

From the definition of $\mathcal{H}_t$ (see equation 1), if $|0\rangle$ is a classical state, we get:

$$\mathcal{H}_t |0\rangle = -t \sum_{X \in \{X\}} |X\rangle \tag{26}$$

where $\{X\}$ is the set of the classical states which is available from $|0\rangle$ with the flipping of a single plaquette. Therefore we can easily calculate the following expressions using the definition of g (see equation (15)):

$$\langle 0|\mathcal{H}_t|0\rangle = 0 \ , \tag{27a}$$

$$g\mathcal{H}_t |0\rangle = \sum_X \frac{1}{E_0 - E_X} |X\rangle \langle X| \mathcal{H}_t |0\rangle \ , \tag{27b}$$

Let us express the correction to the fourth order - from equation (14) with substituting $V{=}\mathcal{H}_t$ and using the lemmas (27). The first two order corrections are

$$\varepsilon^{(1)} = \langle 0|\mathcal{H}_t|0\rangle = 0 \ , \tag{28a}$$

$$\varepsilon^{(2)} = \langle 0|\mathcal{H}_t g \mathcal{H}_t|0\rangle = \sum_X \frac{1}{E_0 - E_X} \langle 0| \mathcal{H}_t |X\rangle \langle X| \mathcal{H}_t |0\rangle \ . \tag{28b}$$

At the third-order correction, we should note that two different classical states of $\{X\}$ are not connected with a simple plaquette flipping. Therefore we can write

$$\begin{aligned} \varepsilon^{(3)} &= \langle 0|\mathcal{H}_t g \mathcal{H}_t g \mathcal{H}_t|0\rangle - \langle 0|\mathcal{H}_t|0\rangle \langle 0|\mathcal{H}_t g^2 \mathcal{H}_t|0\rangle = \\ &= \sum_{X_1, X_2 \in \{X\}} \frac{1}{(E_0 - E_{X_1})(E_0 - E_{X_2})} \langle 0| \mathcal{H}_t |X_1\rangle \langle X_1| \mathcal{H}_t |X_2\rangle \langle X_2| \mathcal{H}_t |0\rangle = 0 \end{aligned} \tag{29}$$

Finally, we can write the fourth-order correction in the following form:

$$\begin{aligned} \varepsilon^{(4)} &= \langle 0|\mathcal{H}_t g \mathcal{H}_t g \mathcal{H}_t g \mathcal{H}_t|0\rangle - \langle 0|\mathcal{H}_t g \mathcal{H}_t|0\rangle \langle 0|\mathcal{H}_t g^2 \mathcal{H}_t|0\rangle = \\ &= \sum_X \sum_{Y_X} \frac{1}{(E_0 - E_X)^2 (E_0 - E_{Y_X})} \langle 0| \mathcal{H}_t |X\rangle \langle X| \mathcal{H}_t |Y_X\rangle \langle Y_X| \mathcal{H}_t |X\rangle \langle X| \mathcal{H}_t |0\rangle \\ &\quad - \left(\sum_X \frac{1}{(E_0 - E_X)^2} \langle 0| \mathcal{H}_t |X\rangle \langle X| \mathcal{H}_t |0\rangle \right) \left(\sum_X \frac{1}{E_0 - E_X} \langle 0| \mathcal{H}_t |X\rangle \langle X| \mathcal{H}_t |0\rangle \right) \ , \end{aligned} \tag{30}$$

where $|Y_X\rangle$ is a classical state which is available from $|X\rangle$ by a single plaquette flipping, and $|Y_X\rangle \neq |0\rangle$.

References

[1] A. D. King, C. Nisoli, E. D. Dahl, G. Poulin-Lamarre, and A. Lopez-Bezanilla, "Qubit spin ice," *Science*, vol. 373, no. 6554, p. 576–580, Jul 2021. [Online]. Available: http://dx.doi.org/10.1126/science.abe2824

[2] N. Shannon, G. Misguich, and K. Penc, "Cyclic exchange, isolated states, and spinon deconfinement in an xxz heisenberg model on the checkerboard lattice," *Physical Review B*, vol. 69, no. 22, Jun 2004. [Online]. Available: http://dx.doi.org/10.1103/PhysRevB.69.220403

[3] J. D. Bernal and R. H. Fowler, "A theory of water and ionic solution, with particular reference to hydrogen and hydroxyl ions," *The Journal of Chemical Physics*, vol. 1, no. 8, pp. 515–548, 1933. [Online]. Available: https://doi.org/10.1063/1.1749327

[4] L. Pauling, "The structure and entropy of ice and of other crystals with some randomness of atomic arrangement," *Journal of the American Chemical Society*, vol. 57, no. 12, pp. 2680–2684, 1935. [Online]. Available: https://doi.org/10.1021/ja01315a102

[5] P. W. Anderson, "Ordering and antiferromagnetism in ferrites," *Phys. Rev.*, vol. 102, pp. 1008–1013, May 1956. [Online]. Available: https://link.aps.org/doi/10.1103/PhysRev.102.1008

[6] A. P. Ramirez, A. Hayashi, R. J. Cava, R. Siddharthan, and B. S. Shastry, "Zero-point entropy in 'spin ice'," *Nature*, vol. 399, no. 6734, p. 333–399, May 1999. [Online]. Available: https://doi.org/10.1038/20619

[7] E. H. Lieb, "Exact solution of the f model of an antiferroelectric," *Phys. Rev. Lett.*, vol. 18, pp. 1046–1048, Jun 1967. [Online]. Available: https://link.aps.org/doi/10.1103/PhysRevLett.18.1046

[8] D. S. Rokhsar and S. A. Kivelson, "Superconductivity and the quantum hard-core dimer gas," *Phys. Rev. Lett.*, vol. 61, pp. 2376–2379, Nov 1988. [Online]. Available: https://link.aps.org/doi/10.1103/PhysRevLett.61.2376

[9] A. Messiah, *Quantum mechanics: Volume 2*. North-Holland, 1986.

[10] J. R. Baxter, *Exactly Solved Models in Statistical Mechanics*. Academic, 1982.